Enhancement of linear and second-order hyperpolarizabilities in wedge-shaped nanostructures

J. Jayabalan, Manoranjan P. Singh, and K. C. Rustagi
Laser Physics Division, Centre for Advanced Technology, Indore 452013, India
(Received 2 January 2003; revised manuscript received 22 April 2003; published 28 August 2003)

Analytical solutions for the wave functions for free electrons inside a wedge-shaped quantum dot are reported. For silver wedge-shaped quantum dots, linear and second-order hyperpolarizabilities are calculated for various apex angles. It is found that linear and nonlinear hyperpolarizabilities both increase with decreasing apex angle.

DOI: 10.1103/PhysRevB.68.075319 PACS number(s): 73.21.La, 73.22.Dj, 42.65.An

I. INTRODUCTION

Nonlinear optical properties of metallic nanoparticles strongly depend on the local field enhancement[1,2] provided by the plasmon resonance. In spherical metal particles this resonance often occurs in the visible. The resonance frequency is determined by the relation $\varepsilon(\omega)+2\varepsilon_0=0$, where $\varepsilon(\omega)$ is the dielectric function of the metal nanosphere and ε_0 that of the surrounding medium. The field enhancement factor is given by $f=3\varepsilon_0/[\varepsilon(\omega)+2\varepsilon_0]$. The strong enhancement $(|f|^2f^2)^2$ of the degenerate four wave mixing reflectivity predicted by this factor has been experimentally verified.[2] The local field calculations in the quasielectrostatic limit can easily be extended to ellipsoidal particles but for most other shapes computational methods are needed.[3,4] In the context of nonlinear optics, however, most of the experimental work has been performed with close to spherical particles or with particles of unresolved shapes, which are assumed to be spherical. Recently, however, some interesting results have been reported where deviations from spherical shape plays an important role. Lamprecht *et al.*[5] observed second harmonic generation (SHG) from touching nanoparticles placed at the corners of right angle triangles to investigate the dephasing of plasmons. Most interestingly, the second harmonic (SH) signal reduced by nearly a factor of 40 when the triangles were placed in a centrosymmetric arrangement. Since the distance between the triangles was not very small compared to the light wavelength only partial cancellation of the SH contributions from oppositely directed triangles is expected. Much better contrasts in the SHG efficiency should be possible if the triangles are placed closer to each other. In their earlier work, the Graz group have also shown that with electron lithography nanometer size discs of other shapes could also be produced.[6] Very recently, nanoprisms have been made from spherical quantum dots by photoinduced shape modification.[7] Rayleigh scattering was observed in the red from those nanoprisms while the spherical quantum dots from where they are derived, scattered in blue. Two distinct quadrupole plasmon resonances were also seen. Nearly triangular shaped nanodisks were prepared by Keilmann *et al.*[8] by evaporation masked by a close packing hexagonal layer of polystyrene nanospheres. SHG has also been observed from a monolayer of Ga nanoparticles embedded in a transparent SiO_x matrix.[9] While it is expected that metallic clusters of noncentrosymmetric shapes could have a nonvanishing second-order susceptibility, there has so far been no discussions of the mechanisms of optical nonlinearity in such odd shaped clusters.

Higher-order multipole contributions to SHG from spherical nanoparticles as well as their third-order nonlinearities have been investigated in considerable detail.[2,10–12] Since most experiments and theory of third-order effects deal with intensity dependent refractive index, mechanisms other than virtual excitations often play the dominant part.[1,12–14] In contrast, in second-order effects the commonest experiment is SHG, where mechanisms involving thermal effects are not known. Calculation of optical nonlinearities may be performed at various levels of rigor. For small molecules with a few atom first principles calculations are possible. A self-consistent field approach is often more effective for larger molecules or nanoparticles. A calculation of nonlinear response in one-electron approximation with the effective field seen by an electron calculated in the quasielectrostatic approximation has provided very useful insights into the dependence of nonlinear susceptibilities on structure and shape of the electron density. In particular, such models have predicted that the conjugation length of the π electrons in linear molecules and judicious substitution of heteroatoms are two important parameters in optimizing their nonlinear response.[13] Similarly, the particle in a box model together with local field enhancement calculated in the quasistatic approximation has also been used to calculate hyperpolarizability of metal particles[14] and fullerenes.[15]

In the present work, we report similar calculations for a wedge-shaped metallic nanostructure. Since this shape lacks an inversion center, it can have a second-order nonlinear response. Secondly, this shape is a very good approximation for a triangular-shaped quantum dot. Most important, the single particle unperturbed states for this system can be obtained analytically. These solutions are given in Sec. II. In Sec. III we discuss our calculation of linear and nonlinear response of these nanostructures. Conclusions are presented in Sec. IV.

II. GENERAL FORMULATION

We consider a system of N independent electrons confined to a wedge shaped region of radius ρ_0 and apex angle ϕ_0 as shown in Fig. 1. The single particle states are given by

$$H\Psi=E\Psi, \tag{1}$$

with

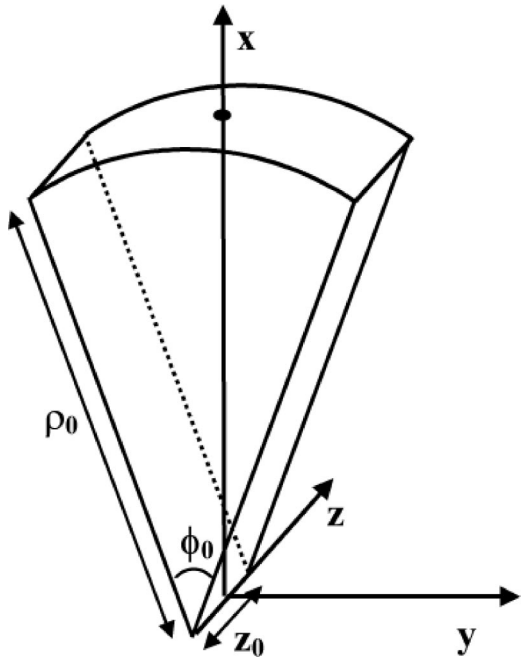

FIG. 1. Wedge-shaped quantum dot.

$$H=-\frac{\hbar^2}{2m}\nabla^2+V(\mathbf{r}), \tag{2}$$

where Ψ is the single particle wave function, m is the effective mass of electron, and the confining potential $V(\mathbf{r})$ is taken such that $V(\mathbf{r})=0$ when $|z|<z_0/2$, $\rho<\rho_0$, and $|\phi|<\phi_0/2$ and $V(\mathbf{r})=\infty$ otherwise. Consequently, the wave function should satisfy the following boundary conditions:

$$\Psi(\pm z_0/2,\rho,\phi)=0,\Psi(z,\rho_0,\phi)=0, \text{ and } \Psi\left(z,\rho,\pm\frac{\phi_0}{2}\right)=0. \tag{3}$$

Solving Eq. (1) with these boundary conditions, the normalized single particle wave functions are

$$\Psi_{\nu,n,s}=\frac{\sqrt{2}}{\sqrt{z_0}}\sin\left(\frac{\nu\pi}{z_0}(z+z_0/2)\right)\psi_{ns}(\rho,\phi), \quad \nu=1,2,3,\ldots, \tag{4}$$

with

$$\psi_{ns}(\rho,\phi)=\frac{2}{\rho_0}\sqrt{\frac{X}{\pi}}\frac{1}{J_{Xn+1}(\alpha_{ns})}J_{Xn}\left(\alpha_{ns}\frac{\rho}{\rho_0}\right)\zeta_n(\phi),$$
$$n=1,2,\ldots, \quad s=1,2,\ldots, \tag{5}$$

where J_{Xn} is the Bessel function of order Xn and α_{ns} is its sth zero, with ϕ_0 defined as

$$\phi_0=\frac{\pi}{X}, \tag{6}$$

where X is an integer. For other values of ϕ_0, Eq. (5) is still valid. The particular choice of ϕ_0 in Eq. (6) results in the computational convenience of dealing with the Bessel functions of the integer order only. The angular part is given by

$$\zeta_n(\phi)=(-1)^{(n+1)/2}\cos Xn\phi \text{ when } n \text{ is odd},$$
$$=(-1)^{n/2}\sin Xn\phi \text{ when } n \text{ is even}. \tag{7}$$

The corresponding eigen energies are

$$E_{\nu ns}=\alpha_{ns}^2E_0+\nu^2E_z, \tag{8}$$

where

$$E_0=\frac{\hbar^2}{2m\rho_0^2} \tag{9}$$

and

$$E_z=\frac{\hbar^2\pi^2}{2mz_0^2}. \tag{10}$$

Having obtained the single particle wavefunctions and energy eigen values for the wedge shape, we turn our attention on to the optical response properties of those wedge shaped metal particles. The linear and nonlinear polarizabilities are calculated using the sum over states perturbation series expansions.[16] The linear polarizability $\alpha_{\sigma\mu}$ which describes the linear refraction and the linear absorption is given by the formula

$$\alpha_{\sigma\mu}=\frac{1}{\varepsilon_o}\sum_{ij}\rho_{ii}^{(0)}\frac{1}{\hbar}\left\{\frac{R_{ij}^{\sigma}R_{ji}^{\mu}}{\omega_{ji}+\omega+i\gamma_{ij}}+\frac{R_{ij}^{\mu}R_{ji}^{\sigma}}{\omega_{ji}-\omega-i\gamma_{ij}}\right\}, \tag{11}$$

and the second-order hyperpolarizability $\beta_{\sigma\mu\lambda}$ for the SHG by the approximation

$$\beta_{\sigma\mu\lambda}(2\omega;\omega,\omega)=\frac{1}{2\hbar^2\varepsilon_o}\sum_{ijk}\rho_{ii}^{(0)}$$
$$\times\left\{\frac{R_{ik}^{\sigma}R_{kj}^{\mu}R_{ji}^{\lambda}+R_{ik}^{\sigma}R_{kj}^{\lambda}R_{ji}^{\mu}}{[\omega_{ki}-2\omega-i\gamma_{ki}][\omega_{ji}-\omega-i\gamma_{ji}]}\right.$$
$$+\frac{R_{ik}^{\lambda}R_{kj}^{\sigma}R_{ji}^{\mu}+R_{ik}^{\mu}R_{kj}^{\sigma}R_{ji}^{\lambda}}{[\omega_{jk}-2\omega-i\gamma_{jk}][\omega_{ki}+\omega+i\gamma_{ki}]}$$
$$+\frac{R_{ik}^{\mu}R_{kj}^{\sigma}R_{ji}^{\lambda}+R_{ik}^{\lambda}R_{kj}^{\sigma}R_{ji}^{\mu}}{[\omega_{kj}+2\omega+i\gamma_{kj}][\omega_{ji}-\omega-i\gamma_{ji}]}$$
$$\left.+\frac{R_{ik}^{\lambda}R_{kj}^{\mu}R_{ji}^{\sigma}+R_{ik}^{\mu}R_{kj}^{\lambda}R_{ji}^{\sigma}}{[\omega_{ji}+2\omega+i\gamma_{ji}][\omega_{ki}+\omega+i\gamma_{ki}]}\right\}, \tag{12}$$

where i and j represents a set of quantum numbers $\{\nu,n,s\}$ characterizing the single particle eigenstates. $\omega_{ij}=(E_i-E_j)/\hbar$ is the energy separation between the two levels i and j, ω is the photon frequency and γ's are the dephasing time constants. σ, λ and μ are Cartesian components. $\rho_{ii}^{(0)}$ is the diagonal density matrix element which corresponds to the population in the level i, R_{ij}^{μ} is the dipole moment matrix

element between the levels i and j along direction μ, and ε_0 is the permittivity of the free space.

For the calculations of $\alpha_{\sigma\mu}$ and $\beta_{\sigma\mu\lambda}$ we need to compute the matrix elements R_{ij}^{x}, R_{ij}^{y}, and R_{ij}^{z}. For the matrix elements along x and y directions we note that this matrix element vanishes when ν' is not equal to ν because of orthogonality of the z part of the wave function. In cylindrical coordinates the matrix elements for x and y direction can be written as

$$R_{ij}=eP_{n;n'}Q_{ns;n's'}, \tag{13}$$

where $P_{n;n'}$ and $Q_{ns;n's'}$ are the angular and radial part of the dipole matrix elements, respectively. The radial part of the transition matrix element for both x and y is given by

$$Q_{ns;n's'}=\frac{2}{\rho_0^2 J_{Xn+1}(\alpha_{ns})J_{Xn'+1}(\alpha_{n's'})}\int_0^{\rho_0}\rho^2 J_{Xn}\times\left(\alpha_{ns}\frac{\rho}{\rho_0}\right)J_{Xn'}\left(\alpha_{n's'}\frac{\rho}{\rho_0}\right)d\rho. \tag{14}$$

The angular part for dipole matrix elements along x direction is given by

$$P_{n;n'}^{x}=\frac{2X}{\pi}\int_{-\pi/2X}^{\pi/2X}\zeta_n(\phi)\zeta_{n'}(\phi)\cos\phi d\phi. \tag{15}$$

It is obvious that $P_{n;n'}^{x}$ is nonzero only when both n and n' are either odd or even integers. Now for the case when n and n' are both odd

$$P_{n;n'}^{x}=(-1)^{(n+n'+2)/2}\frac{1}{\pi}\left[\frac{\sin\left(n+n'+\frac{1}{X}\right)\frac{\pi}{2}}{n+n'+\frac{1}{X}}+\frac{\sin\left(n'-n+\frac{1}{X}\right)\frac{\pi}{2}}{n'-n+\frac{1}{X}}+\frac{\sin\left(n-n'+\frac{1}{X}\right)\frac{\pi}{2}}{n-n'+\frac{1}{X}}+\frac{\sin\left(n+n'-\frac{1}{X}\right)\frac{\pi}{2}}{n+n'-\frac{1}{X}}\right], \tag{16}$$

whereas, for n and n' both even we have

$$P_{n;n'}^{x}=(-1)^{(n+n')/2}\frac{1}{\pi}\left[-\frac{\sin\left(n+n'+\frac{1}{X}\right)\frac{\pi}{2}}{n+n'+\frac{1}{X}}+\frac{\sin\left(n'-n+\frac{1}{X}\right)\frac{\pi}{2}}{n'-n+\frac{1}{X}}+\frac{\sin\left(n-n'+\frac{1}{X}\right)\frac{\pi}{2}}{n-n'+\frac{1}{X}}-\frac{\sin\left(n+n'-\frac{1}{X}\right)\frac{\pi}{2}}{n+n'-\frac{1}{X}}\right]. \tag{17}$$

The angular part for dipole matrix elements along y direction is given by

$$P_{n;n'}^{y}=\frac{2X}{\pi}\int_{-\pi/2X}^{\pi/2X}\zeta_n(\phi)\zeta_{n'}(\phi)\sin\phi d\phi. \tag{18}$$

$P_{n;n'}^{y}$ is nonzero only when one of the subscript is even and another is odd. In this case it is given by

$$P_{n;n'}^{y}=(-1)^{(n+n'+1)/2}\frac{1}{\pi}\left[\frac{\sin\left(n+n'-\frac{1}{X}\right)\frac{\pi}{2}}{n+n'-\frac{1}{X}}+\frac{\sin\left(n-n'+\frac{1}{X}\right)\frac{\pi}{2}}{n-n'+\frac{1}{X}}-\frac{\sin\left(n+n'+\frac{1}{X}\right)\frac{\pi}{2}}{n+n'+\frac{1}{X}}-\frac{\sin\left(n'-n+\frac{1}{X}\right)\frac{\pi}{2}}{n'-n+\frac{1}{X}}\right]. \tag{19}$$

For matrix elements along z direction it is easy to find the conditions $n=n'$ and $k=k'$:

$$R_{ij}^{z}=\frac{2}{z_0}\int_0^{z_0}\sin\left(\frac{\nu\pi z}{z_0}\right)\sin\left(\frac{\nu'\pi z}{z_0}\right)zdz \tag{20}$$

$$=\frac{z_0}{\pi^2}\left[\frac{\cos(\nu-\nu')\pi-1}{(\nu-\nu')^2}-\frac{\cos(\nu+\nu')\pi-1}{(\nu+\nu')^2}\right]. \tag{21}$$

Using these selections rules and the expressions for the transition matrix elements we can calculate the linear and second order hyperpolarizabilities. It follows from the symmetry of the wedge considered here the nonzero components of the second order hyperpolarizability are β_{xxx}, β_{xyy}, β_{xzz}, and their permutations. In this paper we, however, calculate the most important components α_{xx} and β_{xxx}. From simple scaling argument that the dipole matrix element along any direc-

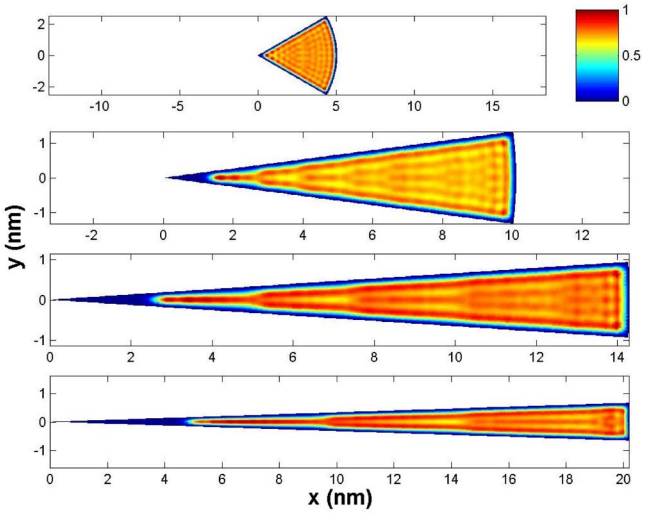

FIG. 2. (Color online) Ground-state electron density distribution in the wedge for 160 electrons and different apex angles. (a) $\phi_0 = \pi/3$. (b) $\phi_0 = \pi/12$. (c) $\phi_0 = \pi/24$. (d) $\phi_0 = \pi/48$.

tion should go as the corresponding length of the wedge, the ratio $|\beta_{xyy}/\beta_{xxx}|$ should behave as $1/X^2$. We will deal with this point more quantitatively later in the paper. Extension of the calculation for other directions and other components of α and β is straight forward.

The wedge shape allows several interesting limiting cases. The three important lengths in the problem are z_0, ρ_0, and $\rho_0\phi_0$. Confinement effects become significant when these lengths become comparable to the de Broglie wavelength of electrons at the Fermi level which is essentially the atomic size. Thus for $z_0 \sim$ atomic diameter, the wedge is a two-dimensional (2D) system—only $\nu = 1$ levels are involved. The limit $\phi_0 \ll 1$, may have some resemblance to a one-dimensional (1D) situation. However, the real situation is more complicated. The electron charge density does resemble that for a linear atomic chain, but it still has substantial influence of the asymmetric boundary condition and the integrated density of states is not close to that for a 1D case. We will come back to this point later in Sec. III while discussing results on linear and nonlinear polarizability.

III. RESULTS AND DISCUSSIONS

A. Electron density

In Fig. 2 we show the electron density for wedges with various apex angles all having 160 electrons with the electron density inside the wedge to be appropriate for bulk Ag. Dimension of the wedge along the z direction is taken to be just sufficient to accommodate a single layer of Ag atoms. Single particle levels are filled according to the Pauli exclusion principle. As mentioned earlier for monolayer thickness along z direction the problem is effectively 2D. The sample was assumed to be at 0° K so that all the levels below the Fermi level are filled and above are empty:

$$\rho_{ii}^{(0)} = 1 \quad \text{for} \quad i \leqslant \text{ Fermi level}, \tag{22}$$

TABLE I. Location and value of the first peak of Im(α_{xx}) for different apex angles.

X	ρ_0 (nm)	Peak position (eV)	Peak value (nm^3)
3	5.05	0.435	13200
12	10.10	0.231	46720
24	14.28	0.167	56330
48	20.20	0.126	89130

$$\rho_{ii}^{(0)} = 0 \quad \text{for} \quad i > \text{ Fermi level}. \tag{23}$$

The ground state electron density distribution $D(\rho,\phi)$ is defined as

$$D(\rho,\phi) = \sum_i \int |\Psi_i(\rho,\phi)|^2 dz, \tag{24}$$

where i runs for all filled levels. We show the electron density distribution in Fig. 2 for various values of the apex angle ranging from $\pi/3$ to $\pi/48$. The corresponding values of ρ_0 are shown in Table I.

From Eq. (5) one can see that the single particle states for a wedge with $\phi_0 = \pi/X$ are a subset of those of $\phi_0 = \pi$. When X increases the order of Bessel function corresponding to the lowest energy state also increases. The Bessel function of higher-order peaks at higher values of the ρ and thus for higher X the wave function also peaks at higher values of ρ remaining nearly zero for lower values of ρ. As a result if we allow only one electron to be inside the wedge it tends to stay away from the apex. This can be understood in terms of the uncertainty principle—to minimize the confinement energy an electron stays away from the apex. However, as the number of electrons increases because of the Pauli exclusion principle one has to fill the upper levels and hence the electron tends to occupy the narrow regime also. Thus the uncertainty principle and Pauli exclusion principle together decide the shape of electron density distribution inside the wedge. In a real physical quantum dot there cannot be any atom in the immediate neighborhood of the apex because the size should be, at least, of the order of the lattice constant. It is interesting to note that the electron density distribution reflects that the electron density is negligible in the edge region. For example, for $\phi_0 = \pi/24$, when ρ is less than 2.5 nm the width in the y direction is less than the lattice constant of silver which is 0.408 nm. However, as ρ increases beyond 2.5 nm it becomes possible to accommodate one or more atoms along y and we have a corresponding increase in the electron density.

B. Linear and nonlinear polarizability

Next we calculate the linear and second-order hyperpolarizabilities. For the calculation of hyperpolarizabilities near resonances in addition to matrix elements we require the values of decay constants. We have taken all the values of γ's to be 0.005 eV so that we can resolve the resonances. The expressions for α_{xx} and β_{xxx} contain a summation over all possible states. However, following the usual practice, we

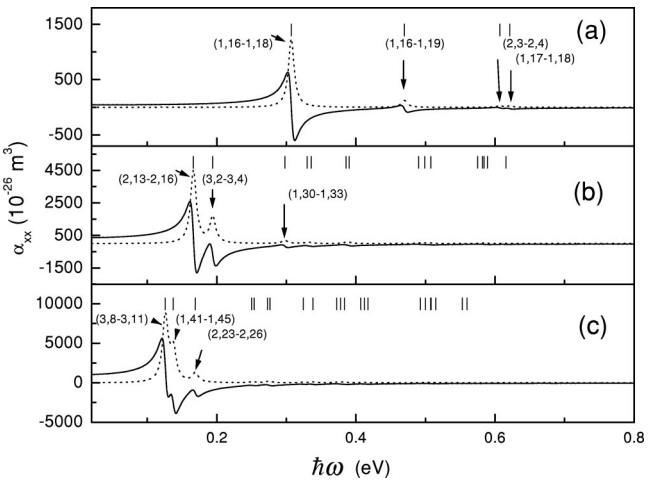

FIG. 3. Real (solid line) and imaginary parts (dotted lines) of α_{xx} as a function of the photon energy for wedges having same apex angle but with different radii. $\phi_0=\pi/48$. (a) $\rho_0=10.1019$. (b) $\rho_0=15.9725$. (c) $\rho_0=20.2038$.

perform the summation over a finite number of states determined by the incident photon energy and the oscillator strength. We also ensure that the results do not change appreciably when additional states are included in the summation.

To study the dependence of α_{xx} on ρ_0 we plot in Fig. 3 the real and imaginary parts of α_{xx} for three different value of ρ_0, 10.1019, 15.9725, and 20.2038 nm having an apex angle of $\pi/48$. The radii of the wedge were chosen such that the upper most level is completely filled. In Fig. 3 we have also shown some of energies of the stronger transitions as bars with the quantum numbers n and s of levels involved in the transition $(n,s\rightarrow n',s')$. We observe that all the stronger transitions are between the levels having same n. This is because the angular contribution of the dipole matrix elements given by Eqs. (16) and (17) both can be approximated, for $X\gg 1$, by

$$P^x_{n;n}\approx\frac{1}{4}\left(1+\frac{1}{4X^2n^2}\right), \tag{25}$$

$$P^x_{n;n'}\approx-\frac{1}{8X^3(n'-n)^2}. \tag{26}$$

Thus,

$$\left|\frac{P^x_{n;n}}{P^x_{n;n'}}\right|\approx 2X^3(n'-n)^2. \tag{27}$$

Hence the transitions between the states having the same angular quantum number n are the dominant transitions for large values of X. Also one can notice in Fig. 3 that as ρ_0 increases all resonances redshift. The amount of red shift is more for the resonances at higher energies. We see from Eq. (9) that the energy is inversely proportional to ρ_0^2. Hence the first resonance red shifts. To see the effect of quantum numbers n and s on the energy, for $s\gg 1$ using the asymptotic behavior of Bessel function we can write

$$\alpha_{ns}\approx s\pi+\left(Xn-\frac{1}{2}\right)\frac{\pi}{2}. \tag{28}$$

For large X the confinement energy in the y direction is very large and the energy levels have a shell structure with shells separated by confinement energy in the y direction which increases as n^2 while energy levels within each shell (same n) increase linearly with the quantum number s rather than s^2 as they would for a rectangular box. Thus, even for very narrow wedge angle, the coupling of the x-y motion has a strong influence on the energy level spectrum. For $X=1$, 2, or 3 there is no shell structure as the confinement lengths in the x and y directions are comparable. For $nX\gg 1$, the expression for the radial part of dipole matrix elements [Eq. (14)] can be written as

$$Q_{ns;ns'}\approx-\frac{4\rho_0\alpha_{ns}\alpha_{ns'}}{(\alpha^2_{ns'}-\alpha^2_{ns})^2},=-4\rho_0E_0\frac{(E_{ns}E_{ns'})^{1/2}}{(E_{ns'}-E_{ns})^2} \tag{29}$$

and

$$Q_{ns;ns}\approx\rho_0\left(1-\frac{1}{2\alpha_{ns}}\right). \tag{30}$$

Thus, the oscillator strength between neighboring levels is the largest and decreases rapidly as the energy separation between the two levels increases. In short, for very small wedge angle most important transition are between the same shell and to that extent situation is like that for a one-dimensional chain.

It is well known that for 1D electron gas most of the oscillator strength lies in the first transition.[17] Because of the confinement along the y direction, in the wedge of apex angle $\pi/48$ and radius 10.1019 nm the electron density in the wedge is similar to that of a linear chain. The hyperpolarizability β is, however, a manifestation of the small deviation from this. As the radius increases, more atoms can be stacked along y direction leading to a two-dimensional atomic distribution.

Next we study the variation of the linear polarizability for different input photon frequencies for wedges having same volume and thickness but different apex angles. In Fig. 4 we show the dependence of α_{xx} on ω for different values of ϕ_0. When the area of the wedge is kept constant and the apex angle is reduced the first absorption peak redshifts. The strength of both real and imaginary parts of α_{xx} at the resonance increases. As ϕ_0 is reduced the length of the wedge along x direction (say L) increases. Since the energy gap between the given two levels goes approximately as $\sim 1/L$, hence there is a redshift. For smaller values of ϕ_0, similar to the earlier case, the strength of the first transition is more than that of the others. But as the apex angle increases the oscillator strength of higher energy transitions also increases. As explained by Eq. (27) the oscillator strength of the transitions having the same n is dominant for the cases having the higher X but as X reduces there are some stronger tran-

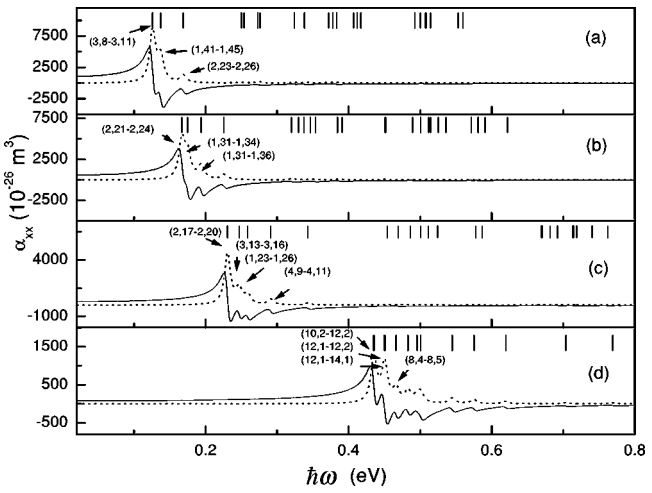

FIG. 4. Real (solid line) and imaginary parts (dotted lines) of α_{xx} as a function of the photon energy for wedges having different apex angles and 160 electrons. (a) $\phi_0=\pi/48$. (b) $\phi_0=\pi/24$. (c) $\phi_0=\pi/12$. (d) $\phi_0=\pi/3$.

sitions between the levels having different n also. For completeness we present in Table I the peak values of the Im(α_{xx}) and the peak positions.

To study the variation of polarizability with the apex angle in the transparency regime we have calculated the real part of α_{xx} for various values of ϕ_0 for a fixed photon energy in the low frequency regime. We have taken the photon energy, $\hbar\omega$ to be 0.02 eV, i.e., below all resonances. The result is shown in Fig. 5. Notice that the linear polarizability increases by an order of magnitude as the apex angle is reduced from $\pi/2$ to $\pi/48$. The figure also shows that the result can be fitted by $\alpha_{xx}\sim X^{-p}$ with $p\approx 0.92$.

As mentioned earlier the main reason for selecting the odd shaped quantum dots is that due to their lack of inversion symmetry they can have nonzero value of even order hyperpolarizabilies. First we calculate the low frequency limit of β (for $\hbar\omega=0.02$ eV). This is shown in Fig. 6 in

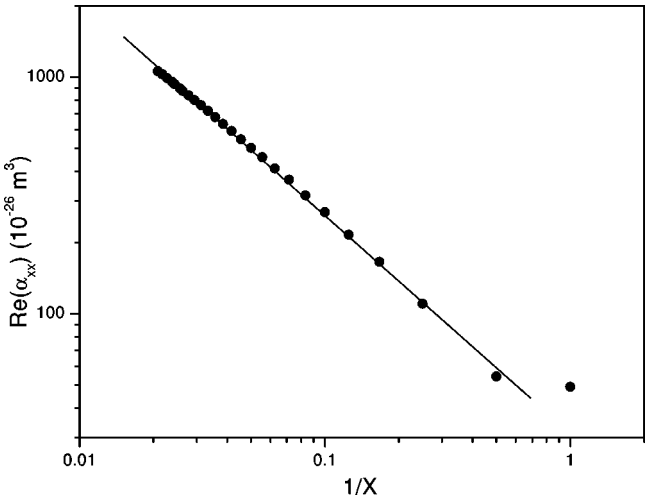

FIG. 5. Re(α_{xx}) as a function of ϕ_0 (solid circles) for 160 electrons inside the wedge. The solid line shows the fit with a function X^{-p} with $p=0.92$.

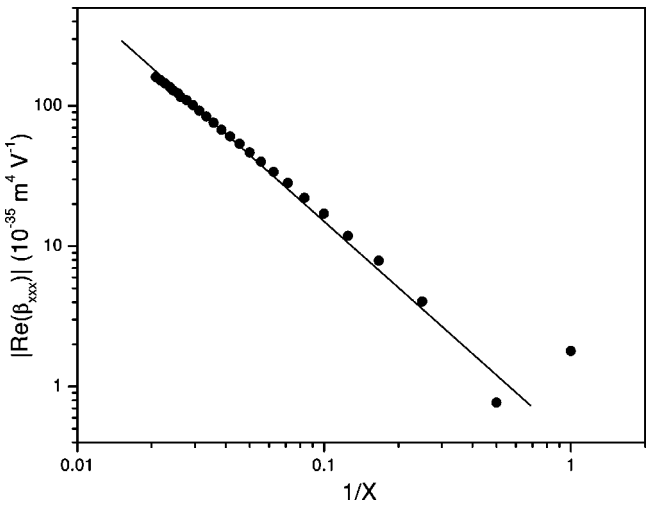

FIG. 6. $|\mathrm{Re}(\beta_{xxx})|$ as a function of ϕ_0 (solid circles) for 160 electrons inside the wedge. The solid line shows the approximate fit with a function X^{-q} with $q=1.57$.

logarithmic scale. β increases by a factor of 200 as ϕ_0 is reduced from $\pi/2$ to $\pi/48$. Thus, as in the linear case, one can enhance the SHG for a given volume of the material by reducing the apex angle. Once again similar to the linear case we find $|\mathrm{Re}(\beta_{xxx})|\sim X^{-q}$ with $q\approx 1.57$. As expected, β varies faster with decrease in ϕ_0. In Fig. 7 we plot the variation of Re(β_{xxx}) with incident field frequency. The second order hyperpolarizability has resonances at the same frequencies as the linear polarizability. Furthermore, it has also smaller peaks at the half frequencies due to the two photon resonances. It is interesting to note that the variation of both α_{xx} and β_{xxx} as a function of ϕ_0 shows a deviation between $\phi_0=\pi/2$ to π from the general trend. The possible explanation may have its origin in the *effective asymmetric area* of the wedge which contributes to these hyperpolarizabilities. The effective asymmetric area can be defined in many ways. We use a simple recipe to find out the effective asymmetric area. The wedge-shaped object is folded at $x=\rho_0/2$ perpendicular to x axis and overlapped with the original object. The

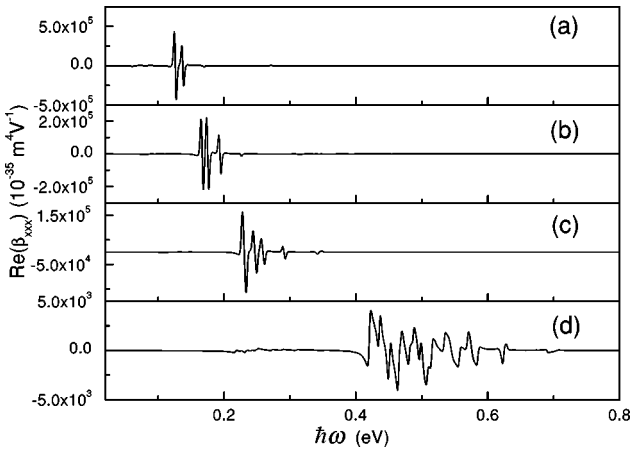

FIG. 7. Re(β_{xxx}) as a function of the photon energy for wedges having different apex angles and 160 electrons. (a) $\phi_0=\pi/48$. (b) $\phi_0=\pi/24$. (c) $\phi_0=\pi/12$. (d) $\phi_0=\pi/3$.

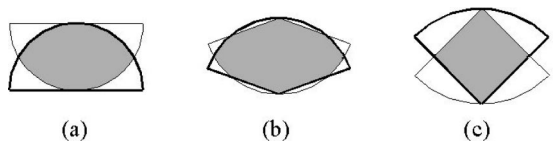

FIG. 8. A simple geometrical construction for calculation of the effective asymmetric area along the x axis for wedge-shaped objects. The object is folded at $x=\rho_0/2$ perpendicular to x axis and overlapped with the original object. The nonoverlapping area gives the asymmetric area which is shown as the unshaded area. (a) $X=1$. (b) $X=1.28$. (c) $X=2$.

nonoverlapping area gives the asymmetric area. We find that the asymmetric area has a minimum at $X=1.28$ (Fig. 8). This qualitatively explains the curves for polarizabilities. At this point it is worth emphasizing that although this simple construction brings out the fact that the degree of asymmetry (along x direction) shows a nonmonotonic behavior as a function of X, this is not the only way to define the asymmetry of shape. However, since another definition of asymmetry also gave similar results, we believe that this result is robust. As mentioned earlier the ratio $|\beta_{xyy}/\beta_{xxx}|$ should decrease strongly as X is increased. Figure 9 shows the ratio $|\beta_{xyy}/\beta_{xxx}|$ at zero frequency as a function of X. The ratio actually goes as $X^{-4.7}$. This is because the selection rules for $P^x_{n;n'}$ and $P^y_{n;n'}$ are different. For $X\gg 1$ matrix elements of y is zero for $n=n'$ and for $n\neq n'$ given by Eq. (19) can be approximated as

$$P^y_{n;n'}\approx -\frac{1}{\pi X^2(n'-n)^2}. \tag{31}$$

From Eqs. (26) and (31) the ratio $P^y_{n;n'}$ to $P^x_{n;n}$ goes as X^{-2}. In contrast the dominant terms for x component of transition dipole matrix element correspond to $n=n'$. Thus the matrix elements of x dominates over y. Thus the ratio of $|\beta_{xyy}/\beta_{xxx}|$ will go more or less as X^{-4}. Additional dependence on X comes because of the changes in the density of states with X.

C. Local field factors

So far we have neglected the difference between the external applied field and the field inside the wedge. As mentioned before this difference in the field inside and the applied field is an important factor in enhancing the nonlinearity of the quantum structure near a plasmon resonance. At nonresonant frequencies the local field factor can be much smaller than unity due to the screening of the external electric field. The local field factor is analytically calculable only for a few geometries, e.g., sphere and ellipsoid. Calculation for the local field factor for the wedge shape is difficult and is not attempted here. However, to have an estimate of the local field factor, the wedge-shaped quantum dot may be approximated by an ellipsoid. This is a good approximation considering that the electron density at the tips of the wedge is nearly zero (Fig. 2), allowing us to neglect any material effects at the tips. For a particle which is small compared to the wavelength of the light, i.e., $\rho_0 \ll \lambda$, the calculated local field correction factor for a dynamic field

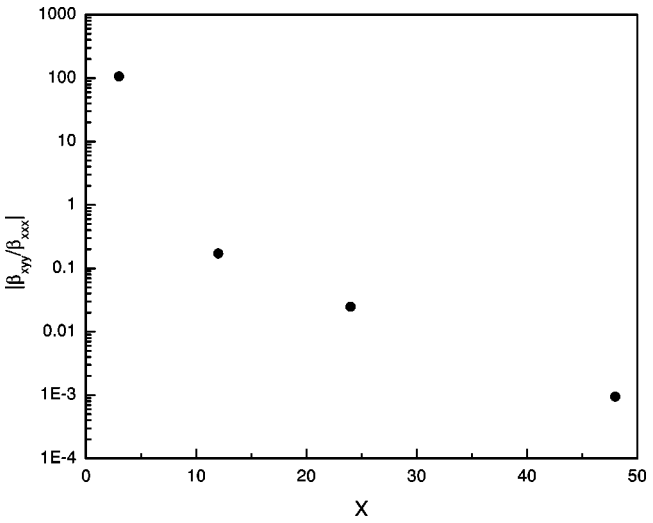

FIG. 9. The ratio $|\beta_{xyy}/\beta_{xxx}|$ at zero frequency as a function of X.

is well approximated in the quasistatic limit. The local field factor in the quasielectrostatic limit for an ellipsoid of semiaxes a, b, and c in the x direction is given by[18]

$$f_{xx}=\frac{\varepsilon_h}{\varepsilon_h+L_x(\varepsilon_{xx}(\omega)-\varepsilon_h)}. \tag{32}$$

Here, ε_h is the dielectric constant of the surrounding medium in which the wedge is embedded and $\varepsilon_{xx}(\omega)$ is the dielectric constant of the medium in the wedge which is related to the polarizability α_{xx}. L_x is the depolarization factor in the x direction and is given by

$$L_x=\frac{abc}{2}\int_0^\infty \frac{dq}{(a^2+q)^{3/2}(b^2+q)^{1/2}(c^2+q)^{1/2}}. \tag{33}$$

For a spherical particle the depolarization factor is 1/3. The field $\vec{E}_{\rm in}$ inside the ellipsoid is given by

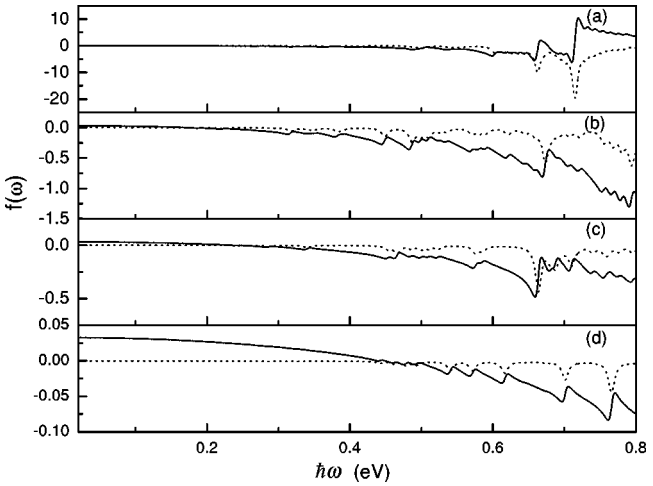

FIG. 10. Real (solid lines) and imaginary parts (dotted lines) of local field enhancement factor as a function of photon energy for wedges having 160 electrons and different apex angles. (a) $\phi_0=\pi/48$. (b) $\phi_0=\pi/24$. (c) $\phi_0=\pi/12$. (d) $\phi_0=\pi/3$.

$$\vec{E}_{\text{in}} = f_{xx}\vec{E}_{\text{out}}, \tag{34}$$

where E_{out} is the external applied electric field.

First we fit an ellipse inside the 2D wedge for different apex angles $\pi/3$, $\pi/12$, $\pi/24$, and $\pi/48$ which gives the values of a and b for the ellipsoid. We take the value of c to be half of the thickness of the wedge along z direction ($c = 0.144$ nm). By assuming the wedge in free space ($\varepsilon_h = \varepsilon_0$) we have calculated the local field factor for various frequencies. We show the variation of the local field factor with the energy of incident photons for various apex angles in Fig. 10. It can be seen from Eq. (32) that whenever the value of $\varepsilon_{xx}(\omega)$ becomes such that

$$\varepsilon_{xx}(\omega) \simeq \varepsilon_h\left(1 - \frac{1}{L_x}\right) \tag{35}$$

the local field factor will become large. Thus the field inside the wedge becomes much higher than the applied external electric field.

IV. CONCLUSION

In conclusion we have shown that the single particle states for a wedge-shaped quantum dot can be found analytically in the free electron model. We have calculated the electron density distribution inside such wedge-shaped dots and shown that the electron density near edges, especially near the apex is almost zero. We have studied the dependence of the linear polarizability on the radius of the wedge for a given apex angle. It increases as the radius increases. As the apex angle is reduced from $\pi/2$ to $\pi/48$ we find an enhancement of an order of magnitude in linear polarizability in the low-frequency limit and this enhancement is 200 for the case of second-order hyperpolarizability. We have also estimated the local field factor for the wedge-shaped quantum dots approximating these by the equivalent ellipsoids.

To determine the structure property relationship for hyperpolarizability β, it is quite appropriate to consider the low frequency limit. However, in the same limit the local field factor is rather small making the effective nonlinear susceptibility also quite small. Large nonlinearities would occur only close to the plasmon resonances. For very small apex angles the field enhancement is large far away from the main resonance in β_{xxx} whereas for larger apex angles wedges both can be simultaneously large. Our calculation also suggest that the organic molecules with large conjugated linear chain with a polarizable unit similar to a phenyl group at one end are expected to have large β.

[1] U. Kreibig and M. Vollmer, *Optical Properties of Metal Clusters* (Springer, Berlin, 1995).

[2] V. Degiorgio and C. Flytzanis, *Nonlinear Optical Materials: Principles and Applications* (IOS Press, Amsterdam, 1995).

[3] C.F. Bohren, in *Handbook of Optics*, 2nd ed., edited by M. Bass (McGraw-Hill, New York, 1995), Vol. 1, Chap. 6, pp. 6.1–6.21.

[4] J.P. Kottmann, D.J.F. Martin, D.R. Smith, and S. Shultz, Opt. Express **6**, 213 (2000).

[5] B. Lamprecht, A. Leitner, and F.R. Aussenegg, Appl. Phys. B: Lasers Opt. **68**, 419 (1999).

[6] W. Gotschy, K. Vonmetz, A. Leitner, and F.R. Aussenegg, Appl. Phys. B: Photophys. Laser Chem. **63**, 381 (1990).

[7] R.J. YunWel, C. Chad, A. Mirkin, K.L.K. George, C. Schatz, and J.G. Zheng, Science **294**, 1901 (2001).

[8] R. Hillenbrand, B. Knoll, and F. Keilmann, J. Microsc. **202**, 77 (2001).

[9] A.M. Malvezzi, M. Patrini, A. Stella, P. Tognini, P. Cheyssac, and R. Kofman, Eur. Phys. J. D **16**, 321 (2001).

[10] F. Hache, D. Ricard, and C. Flytzanis, J. Opt. Soc. Am. B **3**, 1647 (1986).

[11] F. Hache, D. Ricard, C. Flytzanis, and U. Kreibig, Appl. Phys. B: Photophys. Laser Chem. **47**, 347 (1988).

[12] L.M. Ramaniah, S.V. Nair, and K.C. Rustagi, Proc. Solid State Physics Symposium. **33C**, 133 (1991).

[13] S.C. Mehendale and K.C. Rustagi, Opt. Commun. **28**, 359 (1979).

[14] S.V. Nair, Ph.D. thesis, Devi Ahilya Vishwaridyalaya, Indore, India, 1993.

[15] K.C. Rustagi, L.M. Ramaniah, and S.V. Nair, Proc. SPIE **2284**, 90 (1994).

[16] R.W. Boyd, *Nonlinear Optics* (Academic Press, Boston, 1992).

[17] D.A.B. Miller, D.S. Chemla, and S. Schmitt-Rink, Appl. Phys. Lett. **52**, 2154 (1988).

[18] C.F. Bohren and D.R. Huffman, *Absorption and Scattering of Light by Small Particles* (John Wiley & Sons, New York, 1983).